Materials Today Nano 34 (2026) 100828

Contents lists available at ScienceDirect

Materials Today Nano

journal homepage: www.sciencedirect.com/journal/materials-today-nano

Bioreducible Cu_2O cluster-glutathione nanohybrids with multienzyme-mimetic ROS scavenging for cisplatin-induced acute kidney injury

Hokyung Lee [a,b,1], Dahye Noh [a,c,1], Young Ahn [a], Kyeong-Min Lee [f], Shin Young Park [a,d], Jiyeon Shin [a,d], Man Kyu Shim [a,c], Sun Hwa Kim [a,d], Tae Il Noh [e], Hyun-Chul Kim [f], Sangmin Lee [b], Kwangmeyung Kim [g], Hwa Seung Han [f,*], Hong Yeol Yoon [a,c,**]

[a] Medicinal Materials Research Center, Biomedical Research Division, Korea Institute of Science and Technology (KIST), 5 Hwarang-ro 14-gil, Seoul, 02792, Republic of Korea
[b] Department of Fundamental Pharmaceutical Sciences, College of Pharmacy, Kyung Hee University, 26 Kyungheedae-ro, Seoul, 02447, Republic of Korea
[c] Division of Bio-Medical Science & Technology, KIST School, University of Science and Technology, 5 Hwarang-ro14-gil, Seoul, 02792, Republic of Korea
[d] KU-KIST Graduate School of Converging Science and Technology, Korea University, 145 Anam-ro, Seoul, 02841, Republic of Korea
[e] Department of Urology, Anam Hospital, Korea University College of Medicine, 73, Goryeodae-Ro, Seoul, 02841, Republic of Korea
[f] Division of Biomedical Technology, Daegu Gyeongbuk Institute of Science and Technology (DGIST), 333 Techno Jungang-daero, Daegu, 42988, Republic of Korea
[g] College of Pharmacy, Graduate School of Pharmaceutical Sciences, Ewha Womans University, Seoul, 03760, Republic of Korea

ARTICLE INFO

Keywords:
Cisplatin-induced acute kidney injury
Copper oxide nanoparticle
Antioxidants
Bioreducible nanoparticle
Reactive oxygen species scavenger

ABSTRACT

Cisplatin (Cis)-induced nephrotoxicity remains a major clinical challenge, largely driven by reactive oxygen species (ROS)-mediated oxidative stress leading to acute kidney injury (AKI). Because effective therapies for AKI remain limited, antioxidants capable of scavenging ROS and selectively accumulating in injured kidney tissue are highly desirable. Artificial nanocatalysts have emerged as promising antioxidant therapeutics owing to their advantages over natural enzymes. Here, we developed bioreducible nanohybrids (GCuNPs) composed of copper (I) oxide (Cu_2O) nanocatalysts stabilized by glutathione (GSH), synthesized via the reductive reaction of copper ions in the presence of ascorbic acid and GSH. GCuNPs exhibited enhanced broad-spectrum ROS-scavenging capacity and multi-enzyme-like activities *in vitro*. Following systemic administration in a Cis-induced AKI mouse model, GCuNPs preferentially accumulated in injured kidneys through an impaired glomerular filtration barrier and loosening of proximal tubular tight junctions. Immunofluorescence analysis revealed that GCuNPs significantly reduced the expression of KIM-1, a proximal tubular injury marker, while preserving HO-1 expression, indicating attenuation of tubular damage and preservation of endogenous antioxidant defense. Furthermore, GCuNP treatment significantly reduced serum creatinine and blood urea nitrogen levels, improved survival, and showed no noticeable toxicity. These findings highlight GCuNPs as a promising therapeutic strategy for mitigating Cis-induced nephrotoxicity and potentially other oxidative stress-associated kidney disorders.

1. Introduction

Cisplatin (Cis), a widely used chemotherapy agent in clinical settings, has been proven to suppress the growth of various human cancers, including bladder, lung, head and neck, and ovarian [1]. Despite its efficacy, Cis administration is impeded in clinical applications by nephrotoxicity [2,3]. Cisplatin-induced acute kidney injury (AKI), characterized by increased serum creatinine levels and serum blood urea nitrogen, involves proximal tubular injury, oxidative stress, inflammation, and vascular injury in the kidney, and eventually renal dysfunction along with the rapid decrease in glomerular filtration rate [4]. Approximately 30 % of patients taking Cis will develop AKI, which is

* Corresponding author.
** Corresponding author. Medicinal Materials Research Center, Biomedical Research Division, Korea Institute of Science and Technology (KIST), 5 Hwarang-ro 14-gil, Seoul, 02792, Republic of Korea.
E-mail addresses: snaseung@dgist.ac.kr (H.S. Han), seerou@kist.re.kr (H.Y. Yoon).
[1] These authors contributed equally to this work.

https://doi.org/10.1016/j.mtnano.2026.100828
Received 1 December 2025; Received in revised form 13 April 2026; Accepted 23 April 2026
Available online 24 April 2026

responsible for the high rate of morbidity and more than 50 % of mortality [5]. Although dosage reduction and dose discontinuation have been applied to relieve AKI during clinical Cis treatment, the suppression effect of Cis on solid tumors is also reduced [6]. To date, no specific curative therapeutic strategy is available for treating AKI, and the current supportive approaches for AKI have primarily focused on transfusion and blood dialysis, indicating limited potential in efficacious Cis therapies [7]. Therefore, it is highly needed to develop a novel strategy to directly target the unique pathological processes of AKI, providing promising alternatives for the optimized management of AKI.

Oxidative stress is one of the main pathological characteristics contributing to the progression of AKI [8]. It involves the overproduction of reactive oxygen species (ROS), which are intimately associated with the imbalance between ROS and the antioxidant defenses, triggering a cascade of cell death for renal dysfunction [9]. In this regard, efficient ROS scavenging can alter the oxidative stress-mediated pathological microenvironment in AKI and has gained recognition as one of the critical targets of AKI [10–12]. Inspired by this, recent advances in nanomedicine have accentuated the innovative strategies for ROS scavenging and the treatment of ROS-related diseases using various nanomaterials containing copper [13–15], cerium [16,17], carbon [18,19], platinum [20,21], redox polymers [22–24], polyphenols [25], manganese [26], and ruthenium [27]. Among them, ultrasmall nanoparticles (<10 nm) are gaining mounting attention due to their ability, including remarkable ROS clearance by high catalytic activity and preferential renal uptake via passive targeting in AKI [28–31]. However, it is important to consider if the benefits of faster elimination and lower off-target toxicity at the ultrasmall nanostructures outweigh the drawbacks of decreased accumulation at the target site. Therefore, it remains challenging to design nanoantioxidants with high renal targeting ability and low systemic toxicity to treat AKI.

Copper, an essential trace element, is an important cofactor for many enzymes required for metabolic processes [32]. Recent findings have highlighted the crucial roles of copper-based nanomaterials as nanocatalysts due to their unique characteristics, such as a simple manufacturing technique, effective catalytic activity, nanoscale dimension, and improved optical behavior [33]. Notably, the cuprous oxide nanoparticles (Cu_2O NPs) are considerably promising as a versatile and powerful antioxidative platform for the therapy of ROS-related diseases since they not only possess good catalytic activity in scavenging hydrogen peroxide (H_2O_2), superoxide anion (O_2^-), and hydroxyl radicals (•OH) but also promote electron transfer reaction, thereby showing broad-spectrum enzymatic activity and enhanced antioxidant effects [34,35]. These findings have enabled new ways to prevent tubular function from ROS damage by mimicking the intracellular antioxidant enzyme-based defense procedure, such as catalase (CAT), superoxide dismutase (SOD), and glutathione peroxidase (GPx) in AKI treatment.

Glutathione (GSH) has garnered significant attention as a versatile protecting ligand in nanomaterials synthesis due to its capacity to form stable covalent bonds with metals beyond its participation in numerous biological processes, including antioxidant [36,37]. Remarkably, the exceptional protective properties of GSH enable the synthesis of ultrasmall atomically precise metal nanoclusters, which demand robust stabilization due to their high surface energy [38,39]. Moreover, the GSH-decorated surfaces not only impart superior biocompatibility to the nanoparticles but also improve stability within biological environments and facilitate cellular uptake into target cells [40]. In addition, the electron-rich functional groups of GSH, as a strong electron donor, promote charge transfer processes for enhanced catalytic efficiency in metal nanomaterials [41]. Given these insights, we hypothesized that ultrasmall Cu_2O-converged bioreducible nanohybrids (GCuNPs), consisting of Cu_2O with a 5 nm diameter as the nanocatalyst and GSH as the robust stabilizer, could be novel candidates as a potential nano-antioxidant by increasing the preferential accumulation in damaged kidney tissue and reducing oxidative stress, thereby improving the survival rate for the treatment of AKI.

Herein, we fabricated the GCuNPs via the reductive reaction of copper ions in the presence of ascorbic acid and GSH, indicating the amorphous Cu_2O clusters in the GSH matrix. The GCuNPs exhibited rapid dissociation in oxidative stress-mimicking H_2O_2 conditions at damaged kidney sites and released ultrasmall Cu_2O nanoparticles in the presence of GSH. Furthermore, the GCuNPs showed higher broad-spectrum ROS scavenging effects and simultaneous enzymatic activities mimicking CAT, SOD, and GPx. The systemically administered GCuNPs successfully accumulated in damaged kidney tissue in a Cis-induced AKI mouse model by an impaired glomerular filtration barrier and facilitated cellular uptake by loosened tight junctions of proximal tubular epithelial cells (PTECs). Finally, the GCuNPs significantly reduced creatinine and blood urea nitrogen levels, leading to increased survival rates without noticeable toxicity (Scheme 1). To the best of our knowledge, this is the first report to describe the ROS scavenging properties of GCuNPs with multi-enzyme-like activity in the AKI mouse model. This therapeutic approach based on GCuNPs would provide a promising nanotherapeutic strategy to improve renal targeting and prevent nephrotoxicity, facilitating the clinical application of GCuNPs-based treatment for AKI.

2. Result and discussion

2.1. Synthesis and characterization of GCuNPs

GCuNPs were prepared using the simple wet chemical method. The synthesis process could be monitored by the changes in the solution color (Fig. 1A). The interaction of blue copper ions and ascorbic acid at pH 8.5 at 80 °C caused the solution to turn sequentially blue, white, and yellow, in which the reduction of copper ions started [42]. CuNPs were incubated for 12 h at 80 °C without GSH addition as a control nanoparticle. To fabricate the GCuNPs, we added an excess amount of GSH to the yellow color solution, followed by incubation for 12 h at 80 °C. As shown in Fig. 1B, the representative color of the solutions changed from yellow-brown to red-brown and dark brown, indicating successful formation of the Cu_2O in the reductive condition in both CuNPs and GCuNPs. The hydrodynamic diameters of CuNPs and GCuNPs were measured to be 146.3 ± 4.1 and 128.1 ± 1.0 nm, respectively (Fig. 1C and Fig. S1A). Additionally, they displayed a surface charge of −19.9 ± 0.9 mV and −22.6 ± 1.2 mV, respectively, indicating good colloidal stability (Fig. 1D). Notably, the DLS size represents the hydrodynamic diameter of the nanostructures rather than the primary crystallite size. TEM and high-magnification TEM images reveal that CuNPs exhibit a dense, monolithic morphology, whereas GCuNPs consist of ultrasmall nanocrystalline domains (~5 nm), as evidenced by distinct lattice fringes, assembled into larger secondary nanoclusters (Fig. S2).

The selected area electron diffraction (SAED) analysis revealed that the structural differences between CuNPs and GCuNPs (Fig. 1E). The SAED pattern of CuNPs exhibited distinct Bragg reflections/rings that could be indexed to crystalline Cu_2O planes, including (111), (201), and (1–10), indicating a crystalline structure [43]. In contrast, GCuNPs exhibited a broadened, diffuse halo-like ring with markedly attenuated Bragg features, suggesting a significantly reduced long-range order [44]. This poorly crystalline diffraction pattern is consistent with high-magnification TEM observations, which reveal that GCuNPs are composed of ultrasmall nanocrystalline domains (~5 nm) assembled into larger secondary nanostructures via GSH-mediated surface coordination and stabilization. Collectively, these results indicate that GSH modification induces nanoscale structural disorder and domain subdivision rather than simple structural compaction. EDX mapping images confirmed that CuNPs and GCuNPs had similar spherical shapes and were composed of Cu and O elements. As shown in Fig. 1F, GCuNPs clearly showed the presence of carbon (C), nitrogen (N), and sulfur (S) elements in the nanostructure, indicating that GSH successfully decorated CuNPs. The contents of Cu and S were analyzed using ICP, with 6.49 wt% Cu in CuNPs and 9.25 wt% Cu with 0.88 wt% S in GCuNPs.

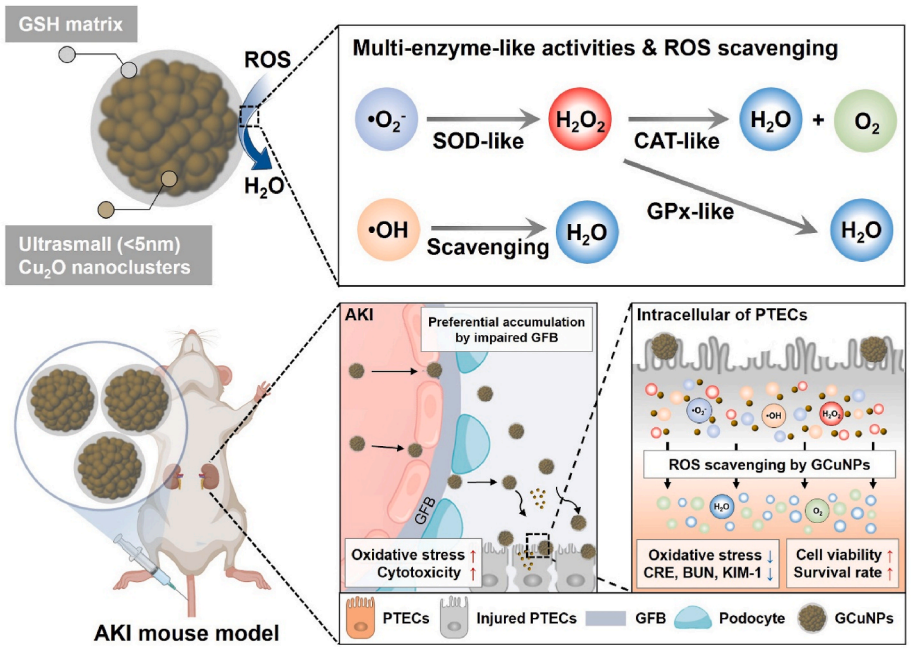

Scheme 1. Schematic illustration of reducing AKI progression by GCuNPs with multi-enzyme-like activities and ROS-scavenging activities in cisplatin-induced AKI. Cu_2O clusters embedded in a GSH matrix, GCuNPs, dissociate ROS into H_2O and O_2 in the damaged kidneys. The GCuNPs exhibit multi-enzyme-mimicking ROS scavenging activity (CAT, SOD, GPx) and preferentially accumulate in injured kidneys of cisplatin-induced AKI mice, enhancing tubular cellular uptake via compromised filtration and tight junctions. Finally, GCuNPs eliminate ROS and relieve oxidative stress in injured PTECs, increasing the cell viability of PTECs and inhibiting AKI progression.

The distinctive structure of GCuNPs might be due to the presence of GSH in controlling crystal growth and structural order: GSH can interfere with crystal growth and promote amorphous structure [45].

The structural properties and oxidation states of CuNPs and GCuNPs were analyzed using powder XRD and XPS, respectively. The XRD spectrum of CuNPs exhibited intense reflections at $2\theta^\circ = 30.0^\circ$, 36.5°, 42.5° and 61.5°, which are indexed to the (110), (111), (200) and (220) planes of the cubic Cu_2O phase (JCPDS 05-0667), respectively. In contrast, the XRD spectrum of GCuNPs exhibited only a broad reflection centered between $2\theta^\circ = 20^\circ$ and 30° (Fig. 1G). This feature is characteristic of an amorphous-like cluster structure lacking long-range lattice order, which results from the ultrasmall size (<5 nm) of Cu_2O nanoparticles stabilized by GSH [46]. The XPS survey scans revealed a core exposure for CuNPs with a prominent Cu 2*p*, Cu LMM, Cu 3*p* signals. In contrast, the XPS survey scan for GCuNPs was dominated by C 1*s* and O 1*s* signals, while the Cu 2*p* peak was significantly reduced (Fig. 1H). This reduced Cu 2*p* peak indicates that the ultrasmall copper oxide nanoparticles in GCuNPs are encapsulated within an organic shell of GSH that exceeds the XPS proving depth [47].

High-resolution XPS spectrums provided additional evidence for the oxidation state of the copper composed for CuNPs and GCuNPs. The Cu $2p_{3/2}$ spectrum of CuNPs showed a primary peak at 933.6 eV with intens shake-up satellites in the 940 – 945 eV range, confirming a surface dominated by Cu^{2+} species formed via ambient oxidation of the Cu_2O core [48]. However, GCuNPs showed a peak at 932.5 eV with negligible satellite peak, confirming that the copper is effectively stabilized in the reduced Cu^+ state within the GSH-protected clusters (Fig. S3A). The O 1*s* spectra further differentiated the surface chemistry, where CuNPs exhibited a peak at 531.5 eV related to the doxide lattice, whereas GCuNPs exhibited a shifted toward higher binding energy (532.2 eV) corresponding to the organic oxygen environments of the carboxyl and amide groups in the GSH (Fig. S3B). Notably, the S 2*p* spectra exhibited a distinct peak at 163 eV for GCuNPs, which is the characteristic peak of metal-thiolate (Cu-S) coordination (Fig. S3C). This stable interfacial anchoring enables to the structural stability of the amorphous nanoclusters and prevents further oxidation. Given the XRD patterns and XPS spectrums, we confirmed that CuNPs as a crystalline Cu_2O@CuO core-shell nanoparticle and GCuNPs as a GSH-stabilized nanocluster including ultrasmall Cu_2O nanoparticles.

To investigate the structural feature of GCuNPs, we monitored the time-dependent size distribution using DLS after the addition of 10 mM GSH. As shown in Fig. 1I, a temporary peak over 1000 nm emerged between 1 h and 3 h of incubation. This phenomenon might be due to the formation of transient solvated aggregates, where the excess GSH molecules act as molecular bridges between the GCuNPs during the initial ligand exchange process [49]. After 6 h of incubation, over the 1000 nm peak completely disappeared, and the size distribution returned to the ultrasmall range (<5 nm). These changes suggest a surface-mediated reorganization and re-dispersion process, where the GSH ligands fully saturate the Cu_2O nanoparticle surfaces. Notably, the solution remained transparent without any significant color change or precipitation (Fig. 1J), indicating that the ultrasmall Cu_2O nanoparticles remained rather than being chemically dissolved. These results further support that nanoclustered structure of GCuNPs, which are formed ultrasmall Cu_2O nanoparticles with GSH.

To investigate the structural stability of GCuNPs, we monitored the changes in nanoparticle size under serum-mimicking conditions, such as 10% FBS-containing PBS (Fig. 1K). CuNPs exhibited a rapid increase in their size as a function of time, resulting from inter-particular aggregation. Interestingly, no significant changes in the particle size of GCuNPs were observed for 4 days in both PBS (pH 7.4) and 10 % FBS-containing PBS (pH 7.4), implying their high resistance to serum protein adsorption by GSH-decorated surfaces [50]. GCuNPs were also observed at predetermined time points to evaluate their degradable behavior in the presence of H_2O_2. As shown in Fig. 1L, the GCuNPs gradually lost their light brown color after 1 h of incubation with 2 mM H_2O_2. Moreover, TEM images of GCuNPs after incubation with H_2O_2 further revealed that the spherical shape of GCuNPs dissociated and reduced the dark area, indicating that Cu_2O in GCuNPs could be degraded by H_2O_2 in a time-dependent manner (Fig. 1M). This result was further supported by the size changes of GCuNPs under the H_2O_2 conditions (Fig. 1N). GCuNPs maintained a stable hydrodynamic

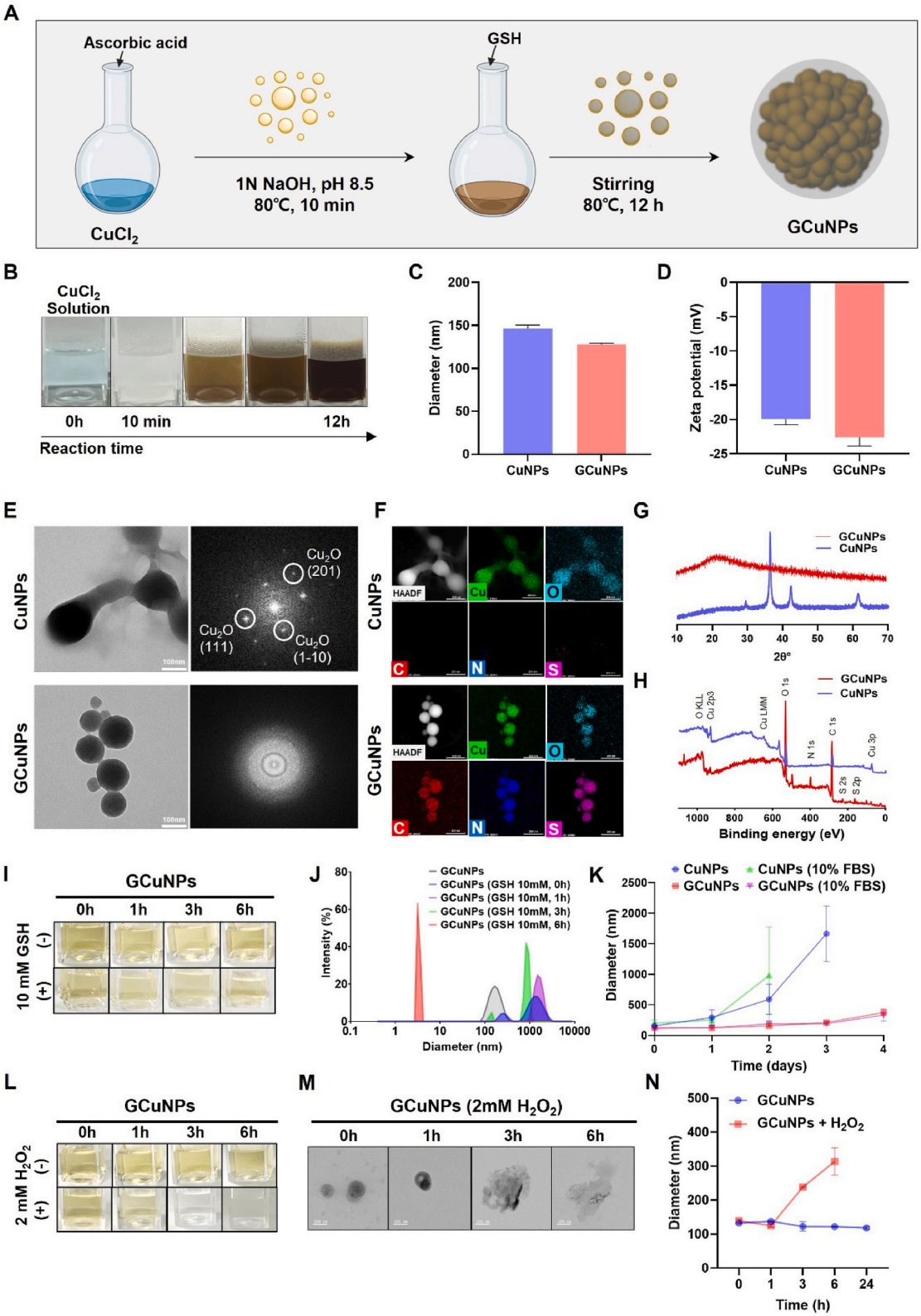

Fig. 1. Preparation and characterization of GCuNPs. (A) Schematic illustration of the preparation of GCuNPs. (B) Time-dependent color changes of reacting solutions. (C) Hydrodynamic diameter of the CuNPs and GCuNPs. (D) Zeta potential of the CuNPs and GCuNPs. (E) TEM images and the SAED patterns of the CuNPs and GCuNPs. The scale bars indicate 100 nm. (F) EDAX mapping images of the CuNPs and GCuNPs. The scale bars indicate 200 nm. (G) XRD spectrums of the CuNPs and GCuNPs. (H) XPS survey scan spectrums of the CuNPs and GCuNPs. (I) Time-dependent color changes of the GCuNPs incubating with 10 mM GSH. (J) Time-dependent size distribution changes of the GCuNPs in 10 mM GSH-containing PBS. (K) Size stability of the CuNPs and GCuNPs in 10 % FBS-containing PBS (pH 7.4) at 37 °C. (L) Time-dependent color changes of the GCuNPs incubating with 2 mM H_2O_2. (M) Time-dependent morphological changes of the GCuNPs incubating with 2 mM H_2O_2, measured by TEM. (N) Time-dependent hydrodynamic diameter changes of the GCuNPs incubating with 2 mM H_2O_2, measured by DLS.

diameter throughout the entire 24-h period, confirming excellent colloidal stability. In the presence of H_2O_2, GCuNPs retained their original size up to 1 h but underwent a rapid size increase from 3 h onward, becoming unmeasurable by 24 h, indicating complete structural disassembly. In comparison, CuNPs without H_2O_2 showed a size increase from 6 h, implying intrinsic colloidal instability in the absence of the GSH coating. In the presence of H_2O_2, CuNPs showed a size increase and color loss from 3 h; however, the magnitude was notably smaller than that of GCuNPs, and the particles remained measurable at 24 h (Fig. S4A and S4B). This can be attributed to the lower H_2O_2 reactivity of the crystalline Cu_2O surface compared to the amorphous GCuNP structure.

Based on the time-dependent TEM observations and DLS measurements, we propose a sequential dissociation mechanism for GCuNPs: (i) H_2O_2 first oxidizes the glutathione coating on the surface of GCuNPs via GPx-like activity while the copper core remains intact; (ii) progressive shell degradation exposes the copper core, which catalyzes H_2O_2 decomposition via CAT-like activity; (iii) Cu^0/Cu^+ is gradually oxidized to Cu^{2+}, leading to core dissolution; and (iv) complete disassembly into soluble Cu^{2+} ions and GSSG fragments, both of which are renally clearable. Notably, the amorphous structure of GCuNPs may further enhance their H_2O_2 reactivity compared to the crystalline Cu_2O structure, due to increased active catalytic sites and structural flexibility [51, 52]. This controlled, multi-stage dissociation mechanism provides sustained, broad-spectrum ROS scavenging during the therapeutic window, while ensuring biocompatibility through ultimate degradation into renally clearable components. These findings provide a mechanistic basis for the enhanced ROS-scavenging performance of GCuNPs observed in subsequent *in vitro* and *in vivo* experiments.

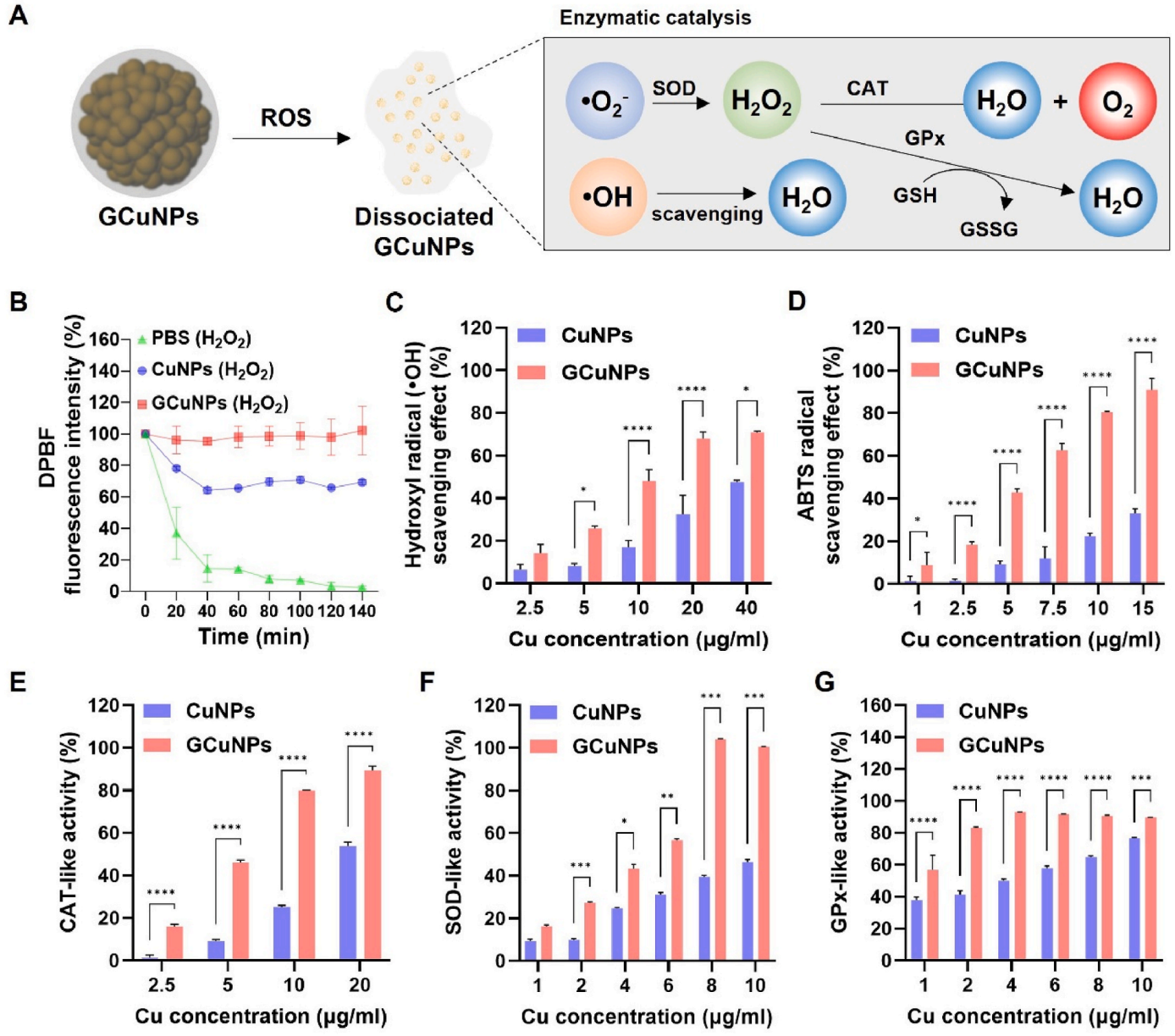

Fig. 2. ROS scavenging and multienzyme-like activity of the GCuNPs. (A) Schematic illustration of ROS scavenging mechanisms of the GCuNPs. (B) H_2O_2, (C) hydroxyl radical, and (D) ABTS radical scavenging effect of the CuNPs and GCuNPs. (E) CAT-like, (F) SOD-like, and (G) GPx-like activity of the CuNPs and GCuNPs. In (B)-(G), data represent means ± S.D. from independent replicates (n = 5). Asterisks *, **, ***, and **** indicate significance level at $p < 0.05$, $p < 0.01$, $p < 0.005$, and $p < 0.001$, respectively.

2.2. ROS scavenging and multienzyme-like activity of the GCuNPs

To further evaluate the ROS scavenging activity of GCuNPs, H_2O_2, •OH, and free radicals generated using ABTS were selected as representative ROS. Furthermore, we also examined CAT, SOD, and GPx-like multi-enzyme activities to evaluate the antioxidant effect of GCuNPs (Fig. 2A).

As shown in Fig. 2B, GCuNPs exhibited significantly enhanced ROS-scavenging activity in a dose-dependent manner. More than 95% of DPBF fluorescence was retained for 140 min in the presence of 2 mM H_2O_2 and GCuNPs (10 μg/ml of Cu), whereas only ~60% was retained under the same conditions with CuNPs. These results indicate that GCuNPs more effectively suppressed H_2O_2-induced oxidative bleaching of DPBF than CuNPs, reflecting the synergistic contribution of the GSH surface to the H_2O_2-scavenging efficiency of the nanozyme. Consistently, the •OH scavenging activities of both GCuNPs and CuNPs increased in a dose-dependent manner. 70.9% and 47.6% of the •OH were scavenged by GCuNPs and CuNPs when Cu concentrations were 40 μg/ml, respectively, showing 1.5-fold higher •OH scavenging activity of GCuNPs compared to CuNPs (Fig. 2C). To evaluate further the antioxidative activity of GCuNPs, a free radical scavenging analysis was performed using ABTS radical assay. As shown in Fig. 2D, ABTS radical scavenging effects gradually increased with the increasing concentration of both GCuNPs and CuNPs. In particular, GCuNPs exhibited more than 2.8-fold higher ABTS radical scavenging effects than CuNPs, resulting in scavenging up to 91.0 % at the Cu concentration of 10 μg/ml. Interestingly, GCuNPs need a 132-fold lower working concentration for ABTS radical scavenging than conventional antioxidant ascorbic acid (AA) [53]. Furthermore, GCuNPs showed lower working concentrations for scavenging H_2O_2 than previously developed nano-antioxidants, such as TiO_2, MnO_2, and Ce, which had 20-50 μg/ml of working concentrations [54–56]. These results supported the idea that GCuNPs had higher antioxidant effects.

In addition to the comprehensive ROS scavenging characteristics, the antioxidant enzyme-like activities of GCuNPs, such as CAT, SOD, and GPx, were investigated. As shown in Fig. 2E, the concentration-dependent CAT-like activity of both GCuNPs and CuNPs was observed, wherein GCuNPs (20 μg/ml of Cu) reacted with up to 89.5 % of 2 mM H_2O_2, exhibiting 1.7-fold higher CAT-like activity than that of CuNPs. Moreover, GCuNPs and CuNPs reduced formazan formation, exhibiting concentration-dependent SOD-like activity (Fig. 2F). Notably, GCuNPs significantly enhanced the SOD-like activity of 2 to 10 μg/ml of Cu concentration, exhibiting up to 2.2-fold higher activity than CuNPs. In addition, GCuNPs exhibited significantly higher GPx-like activity than CuNPs, successfully catalyzing the oxidation of reduced GSH under physiologically relevant conditions (Fig. 2G). These multi-enzyme-like activities of GCuNPs and CuNPs might be based on the broad antioxidant activity of Cu_2O nanoparticles, compared to reported metal oxides such as Fe_3O_4, MnO_2, CeO_2, and V_2O_5 [57].

Importantly, the enhanced antioxidant efficacy of GCuNPs arises not from the independent action of GSH as a standalone antioxidant, but from the synergistic interplay between the Cu_2O domain and the GSH ligand. In the highly oxidative microenvironment of AKI, free GSH would be expected to provide only transient protection, as it is rapidly depleted by stoichiometric oxidation. In contrast, the broad-spectrum antioxidant activity of GCuNPs is primarily attributed to their GSH-stabilized ultrasmall Cu_2O cluster architecture. Specifically, the clustered ultrasmall Cu_2O provides a high density of exposed Cu(I)-rich catalytic sites, where dynamic Cu(I)/Cu(II) redox cycling drives multienzyme-mimetic ROS conversion, including SOD-like superoxide disproportionation, CAT-like H_2O_2 decomposition, and thiol-coupled GPx-like peroxide detoxification [58,59].

Within this framework, GSH functions not merely as a passive coating material, but rather as a thiol-containing stabilizing ligand that preserves cluster integrity, improves colloidal dispersion, and modulates the local coordination and electronic environment of surface Cu sites [60,61]. As demonstrated by our DLS and TEM analyses, GSH-coated GCuNPs maintained structural stability significantly longer than uncoated CuNPs under H_2O_2 conditions, providing direct experimental evidence for this stabilizing role. Collectively, these features indicate that the enhanced renoprotective and antioxidant activity of GCuNPs is well-explained by the high surface redox reactivity of clustered ultrasmall Cu_2O combined with GSH-mediated interfacial stabilization and redox tuning. Accordingly, these structural and catalytic features position GCuNPs as a promising antioxidant nanomaterial for ROS-related diseases.

2.3. In vitro cytotoxicity and ROS scavenging effect of GCuNPs

We also examined the cell viability, cellular uptake, and intracellular ROS scavenging effect of GCuNPs against HK-2 cells, which are PTECs lines and easily damaged by oxidative stress compared to the glomerulus in AKI pathogenesis (Fig. 3A) [62]. Before observing cellular uptake, the cytotoxicity of GCuNPs was preferentially monitored against HK-2 cells using the CCK-8 assay to select the safe concentration range of nanoparticles. As shown in Fig. 3B, both GCuNPs and CuNPs exhibited reduced cell viability at 25 μg/ml of Cu concentration. As a result, we selected a Cu concentration below 12.5 μg/ml, which showed no cytotoxicity, for further *in vitro* cellular experiments.

Given that the pathological processes of the early stage of AKI could be initiated by ROS damage to renal tubules, eliminating intracellular ROS in renal tubule cells is a prerequisite to reducing kidney dysfunction [31]. From this point of view, we first observed the cellular uptake of Cy5.5-labeled GCuNPs against HK-2 cells (Fig. 3C). The red fluorescence signal of GCuNPs gradually increased up to 24 h, which was efficiently uptaken by HK-2 cells compared to CuNPs. Secondly, DCFDA fluorescence signals of GCuNPs were significantly reduced in a dose-dependent manner (Fig. 3D). The quantitative analysis via flow cytometry further supported this signal reduction. As shown in Fig. 3E, the GCuNPs exhibited 22.4 and 12.0-fold lower fluorescence intensity than the non-treated group and CuNPs at 10 μg/ml of Cu concentration, resulting in the enhanced dose-dependent ROS scavenging activity. On the other hand, CuNPs only displayed 1.9-fold lower intensity than the non-treated group at the same concentration. Finally, the intracellular ROS scavenging activity of GCuNPs at 5 and 10 μg/ml of Cu concentration successfully prevented oxidative damage in H_2O_2-treated-HK-2 cells, resulting in 2.3-fold and 2.5-fold higher cell viability compared to H_2O_2-treated cells, respectively. However, the CuNPs only significantly increased the cell viability at 10 μg/ml of Cu concentration (Fig. 3F). These results indicate that GCuNPs are effective in scavenging intracellular ROS, thereby offering enhanced preventive effects against oxidative stress-induced cytotoxicity. While our *in vitro* investigations primarily utilized a general H_2O_2-induced oxidative stress model rather than a cisplatin-induced model. Although the *in vitro* results demonstrate the ROS-scavenging capacity and cytoprotective effects of GCuNPs, the specific cellular interactions and molecular mechanisms of GCuNPs using a cisplatin-challenged renal tubular cells would provide more direct evidence for preventive effects against oxidative stress-induced cytotoxicity.

2.4. In vivo biodistribution of GCuNPs

Subsequently, we monitored the *in vivo* and *ex vivo* tissue distribution of GCuNPs via a near-infrared bioimaging system to assess the effective accumulation in the kidneys of AKI. For the *in vivo* study, we established an AKI mouse model prepared by a one-time intraperitoneal injection of Cis at a dose of 30 mg/kg into balb/c nude mice. Mice were intravenously injected with Cy5.5-labeled CuNPs after 2h of intraperitoneal Cis injection (Fig. 4A). Interestingly, the fluorescence signal of GCuNPs gradually reduced over time in normal mice and that of Cis(+)GCuNPs significantly increased within the kidney region in the AKI mice, exhibiting the strongest fluorescence intensity at 6 h and gradually

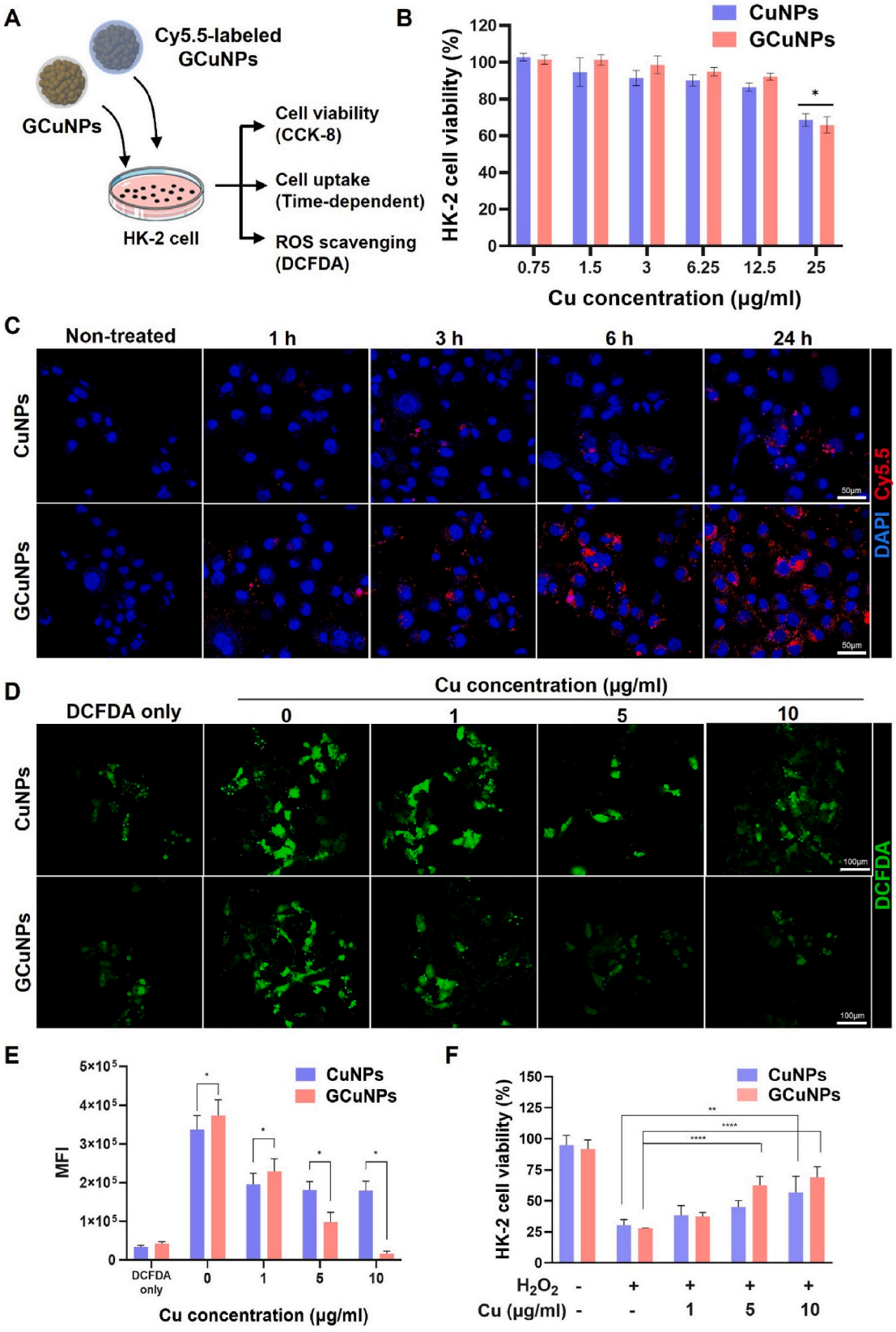

Fig. 3. Cytotoxicity and ROS scavenging effect of GCuNPs *in vitro*. (A) Representative illustration of *in vitro* cellular analysis with GCuNPs. (B) Cytotoxicity of CuNPs and GCuNPs in HK-2 cells under different treatment concentrations. (C) Cellular uptake images of CuNPs and GCuNPs in HK-2 cells, acquired using confocal microscopy (scale bar = 50 μm). (D) Representative ROS staining (DCFDA fluorescence) of HK-2 cells under different treatment concentrations of DCFDA only, CuNPs, and GCuNPs (scale bar = 100 μm). (E) Quantified mean fluorescence intensity (MFI) of DCFDA in HK-2 cells under different treatment concentrations. (F) HK-2 cell viability analysis using CuNPs and GCuNPs in the presence of 2 mM H_2O_2. In (B) and (F), data represent means ± S.D. from independent replicates (n = 5). Asterisks *, **, and **** indicate significance level at $p < 0.05$, $p < 0.01$, and $p < 0.001$, respectively.

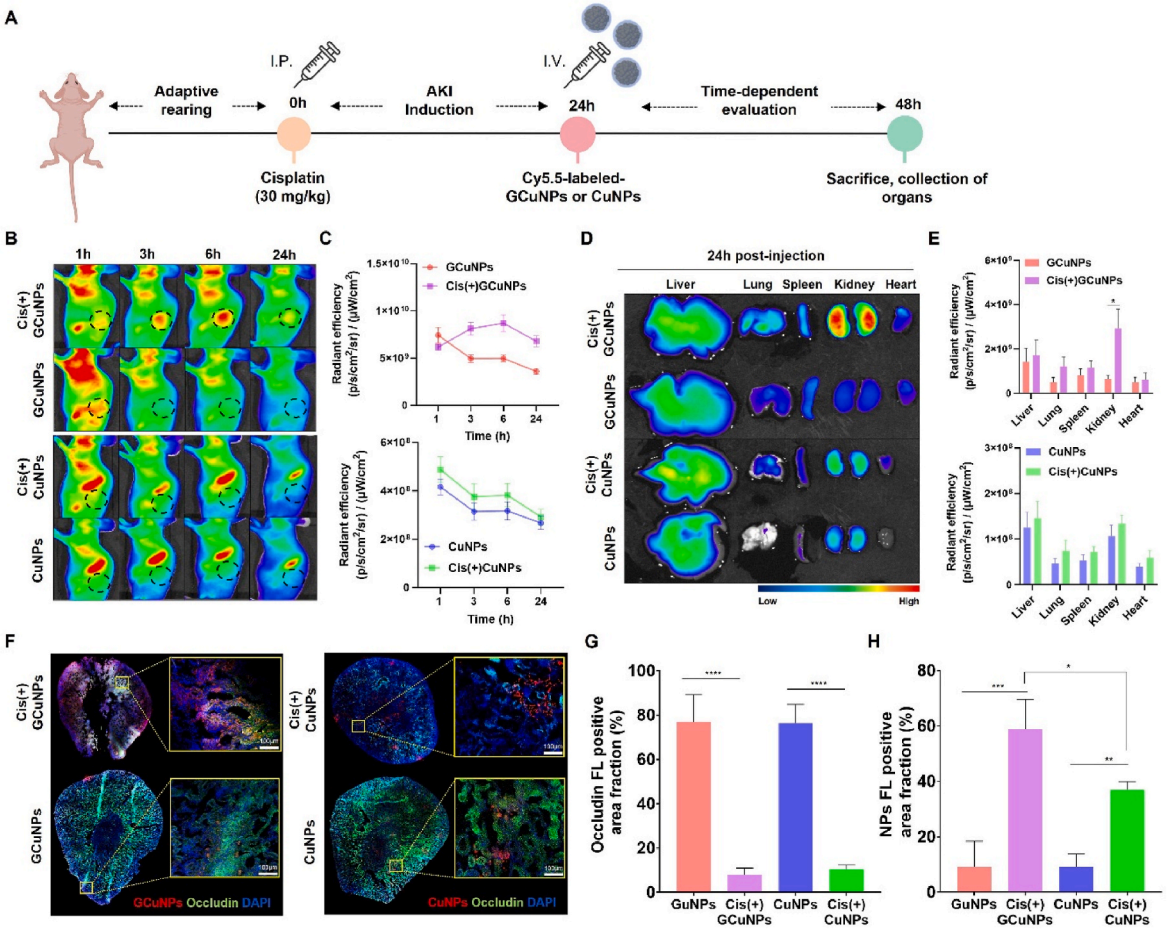

Fig. 4. Biodistribution and kidney accumulation of CuNPs and GCuNPs in cisplatin-induced AKI mice. (A) Schematic illustration of the establishment and imaging schedule of AKI mice. (B) Representative time-dependent whole-body near-infrared fluorescence (NIRF) imaging after treatment of CuNPs and GCuNPs. Dash-line circles indicate the kidney site. (C) Quantified NIRF intensities at the kidney site from (B) (n = 5). (D) Representative *ex vivo* NIRF image of major organs (liver, lung, spleen, kidney, heart) at 24 h post-injection. (E) Quantified NIRF intensities at the major organs from (D) (n = 5). (F) Fluorescence images of kidney tissues stained using the occludin antibody (Red: GCuNPs or CuNPs, Green: occludin (tight junction), Blue: DAPI (nuclei)). (G) Quantified occludin, (H) GCuNPs, or CuNPs fluorescence-positive area fraction, measured by CellProfiler 4.2.7 software. Asterisks *, **, ***, and **** indicate significance level at $p < 0.05$, $p < 0.01$, $p < 0.005$, and $p < 0.001$, respectively.

decreasing at 24 h (Fig. 4B). On the other hand, the fluorescence signals of CuNPs at the kidney region and whole body of both AKI and normal mice gradually decreased over time (Fig. 4C). These results were further supported by *ex vivo* organ imaging at 24 h post-injection (Fig. 4D). The fluorescence signal of Cis(+)GCuNPs were notably 4.5-fold higher than those of the GCuNPs. However, CuNPs didn't show any significant fluorescence differences in the kidney tissues of both AKI and normal mice, resulting in a limited accumulation of CuNPs (Fig. 4E).

To further analyze the distribution of GCuNPs at renal injury sites in AKI, we observed tight junction disruption in the renal tissues using immunofluorescence occludin staining after 24 h post-injection. Occludin is one of the tight junction proteins expressed in the proximal tubule, thick ascending limb, distal convoluted tubule, and collecting duct in the nephron [63]. As shown in Fig. 4F, normal renal tissues had a uniform distribution of occludin compared to the renal tissue in AKI. Notably, Cis(+)GCuNPs mainly accumulated in the cortex of the damaged kidney in Cis-induced AKI, especially around the proximal tubules. Despite tight junction disruption in AKI, CuNPs exhibited limited renal accumulation compared to Cis(+)GCuNPs. On the other hand, both GCuNPs and CuNPs in normal renal tissue partially accumulated around the glomeruli in the cortex. These results correspond with the occludin- and NPs-positive area of Cis(+)GCuNPs, indicating reduced occludin-positive area fraction and increased nanoparticle area fraction (Fig. 4G and H). In particular, Cis(+)GCuNPs exhibited a 1.5-fold higher area fraction than Cis(+)CuNPs in AKI. Overall, this preferential accumulation at the damaged kidney sites after intravenous injection of GCuNPs is presumably due to the destruction of the glomerular filtration barrier (GFB) during AKI development, which allows the passage of large nanoparticles in damaged podocytes in the glomerular capsule [64]. In addition, GCuNPs can specifically target the damaged kidneys with a stealth effect owing to the GSH-decorated surfaces, which could not only improve the serum stability by minimizing the serum protein absorption but also facilitate internalization of nanoparticles into the proximal tubule cells by a sodium ion-dependent system compared to bare CuNPs [50,65]. Therefore, the GCuNPs have an excellent affinity for the damaged kidney in AKI, indicating their significant therapeutic potential in AKI therapy.

2.5. *In vivo* therapeutic efficacy of GCuNPs on cisplatin-induced AKI mice

Next, we evaluated the hemolysis rate of GCuNPs to determine the treatment dose without toxicity. The hemolysis rate of nanomaterials should be less than 5% to ensure safety during intravenous injection [66]. As shown in Fig. 5A and B, GCuNPs exhibited 3.91% and 7.81 % hemolysis rates at 3.75 and 7.5 μg/ml of Cu concentration, respectively. On the other hand, CuNPs gradually increased the hemolysis rate in a Cu concentration-dependent manner, indicating a 26.1 % hemolysis rate at 7.5 μg/ml of Cu concentration. Therefore, we selected the optimal

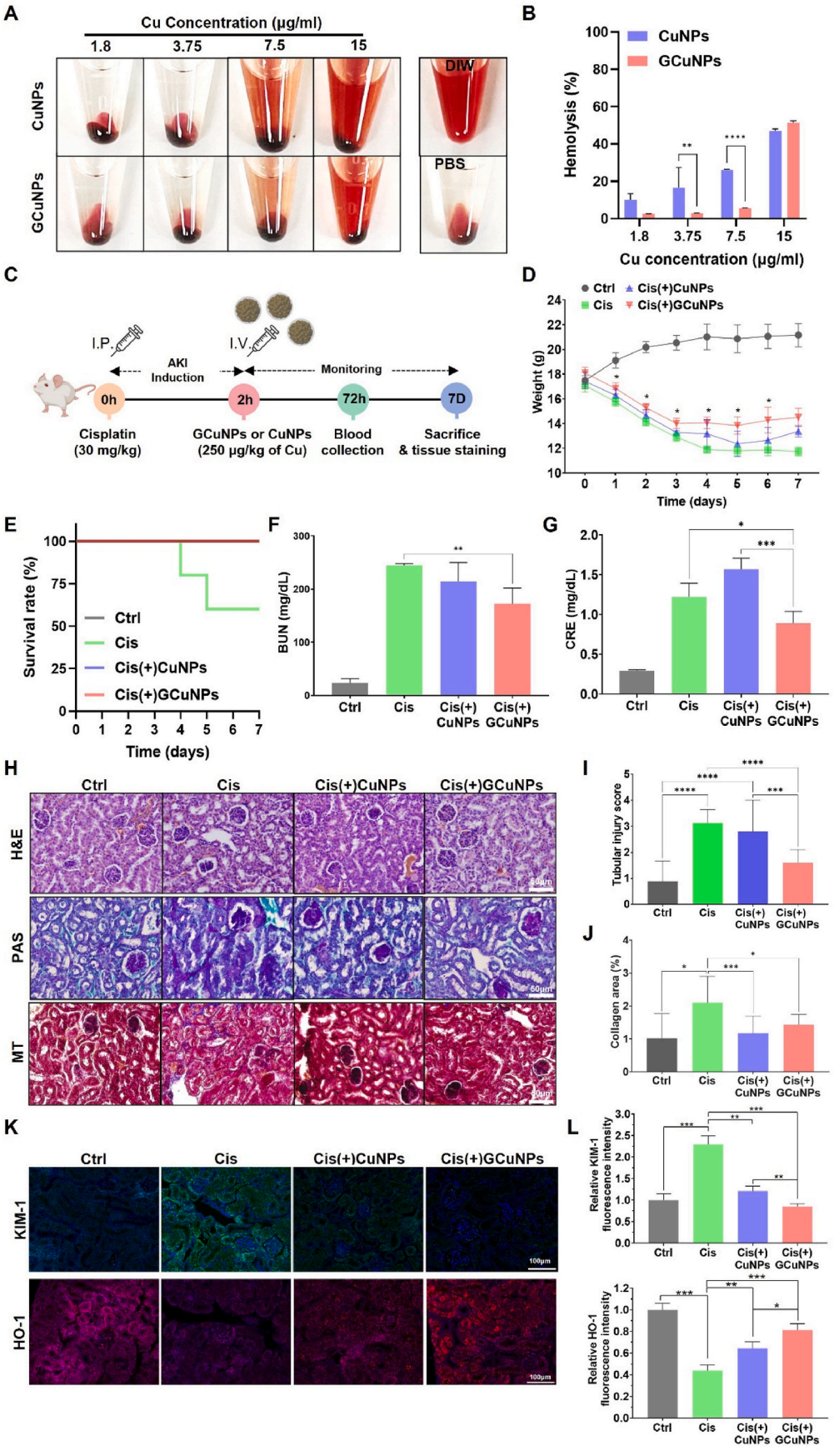

(caption on next page)

Fig. 5. Therapeutic efficacy of GCuNPs on cisplatin-induced AKI mice. (A) Optical images on hemolysis analysis of CuNPs and GCuNPs under different treatment concentrations. (B) Quantified hemolysis rate using a UV-Vis spectrometer. (C) Schematic illustration of the establishment and treatment schedule of AKI mice. (D) Body weight variation of AKI mice for 7 days after different treatments (n = 5). (E) Survival rate of AKI mice with different treatments (n = 5). Serum levels of (F) BUN and (G) CRE in AKI mice at 72 h after different treatments (n = 5). (H) H&E, PAS, and MT staining images of kidney tissues from each group. Scale bars indicate 50 μm. (I) Tubular injury score based on PAS staining images of kidney tissues from each group (n = 10). (J) Collagen deposit area in MT staining images of kidney tissues from each group. (K) Immunofluorescence analysis showing KIM-1 (green fluorescence) and HO-1 (red fluorescence) in the kidney tissues. Blue fluorescence indicates DAPI-stained nuclei (scale bar = 100 μm). (L) Relative fluorescence intensity of KIM-1 and HO-1 in kidney tissues (n = 3). Asterisks *, **, ***, and **** indicate significance level at $p < 0.05$, $p < 0.01$, $p < 0.005$, and $p < 0.001$, respectively.

treatment dose as 250 μg/kg of Cu (corresponding to 5 μg Cu for a 20 g mouse with 1 ml of blood), confirming their excellent biological safety with a hemolysis rate below 5%.

After examining the multi-enzyme-like ROS scavenging and preferential accumulation of GCuNPs at damaged kidney sites, we eventually sought to confirm their therapeutic efficacy in the Cis-induced AKI model as outlined in Fig. 5C and S7. As shown in Fig. 5D, the body weights of the Cis group were severely reduced compared to the normal Ctrl. The Cis(+)GCuNPs group showed the least reduction in body weight loss after Cis injection. Compared with the Cis group, the degree of decrease in the Cis(+)GCuNPs group is significantly higher than that of the Cis(+)CuNPs group. Consistent with these results, survival rates in the Cis(+)GCuNPs group were even higher than those in the Cis group, resulting in a 100% survival rate for 20 days (Fig. 5E and S7C). The serum levels of kidney function indicators such as BUN and CRE demonstrated that the Cis(+)GCuNPs group exhibited a significant drop in both BUN and CRE levels compared to the Cis group (Fig. 5F and G). In particular, the levels of CRE in the Cis(+)GCuNPs group were significantly reduced by 1.8 times compared to the Cis(+)CuNPs group, confirming the excellent therapeutic efficacy of GCuNPs in treating Cis-induced AKI.

Additionally, these results were further supported by histological examination after hematoxylin and eosin (H&E), periodic acid-Schiff (PAS), and Masson's Trichrome (MT) staining (Fig. 5H). H&E staining of kidneys from the Cis group exhibits severe renal tubular damage, as indicated by tubular necrosis, loss of brush borders, and prominent interstitial changes. Notably, these structural damages are markedly ameliorated by the Cis(+)GCuNPs group, suggesting a more effective nephroprotective effect. Furthermore, the tubular injury scores were also significantly lower in the Cis(+)GCuNPs group when compared to the Cis group and Cis(+)CuNPs group (Fig. 5I). In addition, PAS-stained images of the Cis group displayed marked abnormalities such as disrupted tubular architecture and interstitial expansion. In contrast, the Cis(+)GCuNPs significantly attenuated these histological changes, resulting in well-preserved glomerular and tubular structures. These results correspond with the collagen-stained area of the Cis(+)GCuNPs; the collagen-stained area of the Cis(+)GCuNPs group was 1.5 times lower than that of the Cis group (Fig. 5J).

To further evaluate the molecular mechanisms underlying the renoprotective effects of GCuNPs, immunofluorescence (IF) staining for KIM-1 and HO-1 was performed on kidney tissue sections from all experimental groups (Fig. 5K and L, and S6). KIM-1, a well-established proximal tubular injury marker, was markedly upregulated in the Cis group compared to the Ctrl group, confirming severe tubular damage. Both CuNPs and GCuNPs treatment reduced KIM-1 expression, with GCuNPs showing a significantly greater reduction than CuNPs, indicating enhanced protection against tubular cell injury. HO-1, a cytoprotective antioxidant enzyme, was substantially decreased in the Cis group compared to the Ctrl group, reflecting exhaustion of the endogenous antioxidant defense at Day 7. GCuNPs treatment significantly preserved HO-1 expression compared to both the Cis and CuNPs groups, indicating that GCuNPs minimized oxidative damage to the endogenous antioxidant defense system, as reflected by maintained HO-1 levels. Together, the reduction of KIM-1 and the preservation of HO-1 provide complementary molecular evidence supporting the histological observations described above. In summary, these results highlight the potent nephroprotective capabilities of GCuNPs that can mitigate the Cis-induced histopathological changes and preserved the functional integrity of the kidneys by reducing oxidative stress and tubular injury.

2.6. *In vivo biosafety of GCuNPs*

To further evaluation of the systemic biocompatibility of CuNPs and GCuNPs, we performed a comprehensive biosafety evaluation including body weight monitoring, histopathological analysis, and blood chemistry analysis. Notably, biosafety evaluation was performed after 5 times I. V. injection of CuNPs or GCuNPs over 14 days (Fig. S5A). Throughout the treatment, both CuNPs- or GCuNPs-treated groups exhibited a steady increase in body weight without significant fluctuations, compared to Ctrl group (Fig. S5B). The blood chemistry analysis exhibited the levels of major parameters including liver function and renal function. The liver-specific enzymes, such as alanine aminotransferase (ALT), alkaline phosphatase (ALP), and aspartate aminotransferase (AST), in the CuNPs- or GCuNPs-treated group were comparable to those in the Ctrl group, indicating no hepatocellular damage despite the repetitive administration (Fig. S5C). Furthermore, the levels of blood urea nitrogen (BUN) and creatinine showed no significant changes in all groups, indicating no harmful effects in renal function. Other metabolic parameters, including total protein, albumin, and GGT for all groups, also remained within physiological ranges. H&E-stained images of major organs (liver, lung, spleen, kidney, and heart) of GCuNPs-treated group showed no morphological abnormalities, such as inflammatory cell infiltration, congestion, or focal necrosis (Fig. S5D). In contrast, the CuNPs-treated group exhibited minor vacuolar degeneration in hepatocytes, highlighting the superior biocompatibility of GCuNPs. This enhanced safety profile of GCuNPs is likely attributed to the GSH-decorated surface, which provides excellent stability and minimizes off-target interactions in the systemic circulation. In summary, these results demonstrate that the repetitive administration of GCuNPs is functionally and histologically safe within the therapeutic timeframe, providing a robust foundation for their application in treating AKI.

3. Conclusion

In this study, we developed biostable GCuNPs with multi-enzyme-like ROS-scavenging activity, consisting of ultrasmall Cu_2O as the nanocatalyst and GSH as a robust stabilizer, for the treatment of AKI. GCuNPs not only exhibited enhanced broad-spectrum ROS-scavenging capacity but also displayed significantly improved CAT-, SOD-, and GPx-like activities compared to bare CuNPs. Consequently, GCuNPs offered remarkable cellular protection against H_2O_2-induced oxidative damage in HK-2 cells, reflecting their potent antioxidant properties and biocompatibility. In a cisplatin-induced AKI mouse model, systemically administered GCuNPs efficiently accumulated in injured kidney tissue owing to enhanced *in vivo* stability conferred by the GSH-decorated surface. Immunofluorescence analysis further demonstrated that GCuNPs significantly reduced KIM-1 expression while preserving HO-1 levels, confirming attenuation of tubular damage and preservation of endogenous antioxidant defense at the molecular level. Moreover, GCuNPs ameliorated both the histological and functional manifestations of AKI, as evidenced by reduced serum creatinine and blood urea nitrogen levels, improved survival, and no noticeable toxicity. These findings suggest that GCuNPs, a safe and effective antioxidant nanozyme platform, are highly promising as copper oxide-based therapeutics for

the treatment of AKI and other ROS-related intractable diseases.

4. Experimental section

4.1. Materials

All chemicals were used without further purification and purchased commercially. Copper (II) chloride dihydrate ($CuCl_2 \bullet 2H_2O$), L-ascorbic acid (AA), GSH, hydrogen peroxide solution (H_2O_2), 1,3-diphenylisobenzofuran (DPBF, 97%), 2,2-azino-bis (3-ethylbenzothiazoline-6-sulfonic acid) (ABTS), potassium persulfate ($K_2S_2O_8$, 99%), 5(6)-carboxy-2′,7′-dichlorofluorescein diacetate (DCFDA), and Cis hydrochloride, 1N-sodium hydroxide (NaOH) solution, and iron (II) sulfate heptahydrate ($FeSO_4$) were purchased from Sigma Aldrich (St. Louis, MO, USA). Sulfocyanine 5.5-NHS ester (95%) was purchased from Lumiprobe (Wan Chai, Hong Kong). CAT (Cat) activity assay kit and 4′, 6-diamidino-2-phenylindole (DAPI) were purchased from Abcam (Cambridge, MA, USA). The OxiTec™ SOD activity assay kit and OxiTec™ glutathione activity assay kit were purchased from Biomax (Seoul, South Korea). Cell counting kit-8 (CCK-8) was purchased from Dojindo Molecular Technologies, Inc. (Rockville, MD, USA). All chemicals and reagents were of analytical grade and used as received without further purification. Deionized water purified by a Milli-Q system was used throughout the experiment. Dulbecco's Modified Eagle's Medium (DMEM) was purchased from WelGENE Inc. (Daegu, South Korea). Fetal bovine serum (FBS), Opti-MEM™, and Dulbecco's Modified Eagle's Medium/Nutrient Mixture F-12 (DMEM/F-12) were purchased from Gibco™.

4.2. Preparation of GCuNPs and CuNPs

GSH-surface-stabilized copper (I) oxide nanoparticles (GCuNPs) were prepared as previously reported with some modifications [58]. In brief, 336 mg (2.5 mmol) of $CuCl_2$ was dissolved in 50 ml of deionized water and stirred at 85 °C. 4.4g (25 mmol) of L-ascorbic acid was completely dissolved in 50 ml of deionized water and slowly mixed into the $CuCl_2$ solution as a reducing agent. Afterward, the pH of the mixture was adjusted to 8.5 using 1N NaOH solution and stirred for 10 min. For surface stabilization, 1.54g (5 mmol) of GSH was dissolved in 10 ml of deionized water, and then added dropwise to the mixture. The resulting solution was kept stirred at 85 °C for 12 h. After the reaction, the resulting solution was purified by dialysis against deionized water (MWCO = 3500 Da) for 3 days to remove any residues. Finally, the purified solution was centrifuged at 3500 rpm for 30 min, and the supernatant was lyophilized to obtain dark brown powder, GCuNPs. CuNPs were prepared using the same procedure without GSH addition as the control.

For the fluorescent dye labeling, 30 mg of GCuNPs was dispersed in 30 ml of deionized water and mixed with 0.3 mg of Cy5.5-NHS (1 ml in deionized water). As the control nanoparticle, 30 mg of CuNPs was dissolved in 30 ml of deionized water and mixed with 0.3 mg of Cy5.5-GSH (1 ml in deionized water). Each solution was protected from light and stirred for 24 h at room temperature. The solutions were purified using dialysis against deionized water (MWCO = 3500 Da) for 24 h, and the resulting solutions were lyophilized.

4.3. Characterization of GCuNPs and CuNPs

The hydrodynamic diameter, particle size distribution, and zeta potential (ζ) of GCuNPs and CuNPs were measured by dynamic laser scattering (DLS; Nano ZS, Malvern Instruments, UK) at room temperature. The morphology and energy-dispersive X-ray spectroscopy (EDS) mapping images of GCuNPs and CuNPs were observed using transmission electron microscopy (TEM; Talos F200X, FEI Company, USA) at 200 keV. The samples were prepared by dispersing 1 mg/ml of GCuNPs or CuNPs in deionized water. Then, the suspensions were dropped on a carbon-film-coated 200 mesh copper grid. The concentration of copper (Cu) and sulfur (S) was quantified by inductively coupled plasma-optical emission spectrometry (ICP-OES; iCAP 6000 series, Thermo Scientific, USA). Determination of the oxidation states of Cu was observed using an X-ray photoelectron spectrometer (XPS; Nexsa™, Thermo Scientific, USA). GCuNPs and CuNPs were dispersed in PBS and 10 % FBS-containing PBS to observe size stability, followed by measuring particle size for 4 days using DLS. The size changes of GCuNPs and CuNPs by ROS were monitored using DLS at 1, 3, 6, and 24 h post-incubation with 2 mM of H_2O_2 at 37 °C. Furthermore, morphology changes of GCuNPs by H_2O_2 were observed using TEM at 1, 3, and 6 h post-incubation with 2 mM of H_2O_2 at 37 °C. The size changes of GCuNPs by GSH were monitored using DLS at 1, 3, and 6 h post-incubation with 10 mM GSH at 37 °C.

4.4. H_2O_2-scavenging activity assessed by DPBF bleaching assay

The ability of GCuNPs and CuNPs to attenuate H_2O_2-induced oxidative bleaching was assessed by monitoring the fluorescence of 1,3-diphenylisobenzofuran (DPBF) under physiological conditions. Briefly, GCuNPs or CuNPs (10 μg/ml of Cu) were dispersed in PBS (pH 7.4, 1 ml), and 2 μl of DPBF solution (5 mM in DMSO) was slowly added to each sample. Subsequently, 1 μl of H_2O_2 solution (2 M in deionized water) was added to the DPBF-containing PBS, GCuNP, and CuNP samples (final H_2O_2 concentration: ~2 mM). The DPBF fluorescence spectra (λ_{Ex} = 416 nm, λ_{Em} = 445–700 nm) were recorded at predetermined time points using a fluorescence spectrophotometer (F7000, Hitachi High-Technologies, Japan). All measurements were performed under light-protected conditions to prevent photodegradation of DPBF.

4.5. ABTS radical scavenging activity analysis

UV-Vis spectroscopy evaluated the radical scavenging activity of CuNPs and GCuNPs by quantifying the changes from dark blue ABTS radical cation to colorless ABTS. Briefly, 5 mM of ABTS stock solution was mixed with 2 mM potassium persulfate for 6 h in the dark conditions. Then, the ABTS radical solution was diluted using PBS to reach 0.7 absorbance at 734 nm. 1 ml of CuNPs and GCuNPs (1, 2.5, 5, 7.5, 10, 15 μg/ml of Cu) were mixed with 1 ml of ABTS radical solution and further incubated for 10 min. Each sample's absorbances at 732 nm were measured using a microplate reader (VERSAmaxTM; Molecular Devices Corp., USA). Finally, the ABTS radical scavenging activities were calculated as follows:

$$ABTS\ scavenging\ ratio\ (\%) = \left(\left(Abs_{\ Control} - Abs_{\ Sample} \right) \ / \ Abs_{\ Control} \right) x\ 100$$

$Abs_{\ Control}$ represents the absorbance of a standard in the absence of any radical scavengers, while $Abs_{\ Sample}$ indicates the absorbance following the reaction with the radical scavengers.

4.6. ·OH scavenging activity analysis

The •OH scavenging activity was evaluated using the TMB chromogenic method. The Fenton reaction between H_2O_2 and Fe^{2+} generated the •OH. The •OH could oxidize TMB to form oxidized TMB (oxTMB), resulting in a yellow coloration and absorption at 652 nm. In brief, 10 mM $FeSO_4$, 2.5 mM TMB, and 20 mM H_2O_2 were dissolved in DIW as a working solution. Then, 100 μl of working solution was diluted to 900 μl of HAc-NaAC Buffer (0.5M, pH 4.5), and different concentrations of GCuNPs and CuNPs (2.5, 5, 10, 20, 40 μg/ml of Cu, respectively) were mixed with the prepared working solution for 30 min. Finally, the absorption at 652 nm of the solution was measured using a microplate reader.

4.7. CAT-like activity analysis

The CAT-like activity of GCuNPs and CuNPs was evaluated using the

OxiTec™ CAT Activity Assay Kit, in which the Oxi-probe could react with H_2O_2, forming a red complex with an absorbance at 570 nm [67, 68]. In brief, different concentrations of GCuNPs and CuNPs (2.5, 5, 10, 20 μg/ml of Cu, respectively) were incubated with 2 mM H_2O_2 at 25 °C for 1 h. The residual H_2O_2 was then reacted with Oxi-probe and horseradish peroxidase (HRP)-containing working solution for 30 min. Finally, the CAT-like activity of GCuNPs and CuNPs was calculated based on absorbance at 570 nm.

4.8. SOD-like activity analysis

The SOD-like activity of GCuNPs and CuNPs was evaluated using the SOD assay kit (WST-1 method) in different concentrations of GCuNPs and CuNPs (1, 2, 4, 6, 8, 10 μg/ml of Cu, respectively). Two O_2^- were produced by the oxidation of xanthine by xanthine oxidase, forming WST-1 formazan, which was absorbed at 450 nm. The SOD-like activity was calculated using absorbance at 450 nm, which was the method provided by the manufacturer.

4.9. GPx-like activity analysis

The GPx-like activity of GCuNPs and CuNPs was determined using the GPx Assay Kit according to the manufacturer's instructions. In brief, different concentrations of GCuNPs and CuNPs (1, 2, 4, 6, 8, 10 μg/ml of Cu, respectively) were incubated with 5,5′-dithiobis-(2-nitrobenzoic acid) (DTNB) at 37 °C for overnight, monitoring color changes from pale yellow into yellow, which had absorbance at 412 nm.

4.10. Cell culture

The human adult male kidney proximal tubular epithelial (HK-2) cells were purchased from the American Type Culture Collection (ATCC, USA). The HK-2 cells were cultured in Dulbecco's Modified Eagle's Medium/Nutrient Mixture F-12 (DMEM/F-12) enhanced with 10 % FBS and 1 % antibiotic-antimycotic solution (AA). Then, the HK-2 cells were incubated at 37 °C in a humidified incubator with 5 % CO_2.

4.11. Cellular uptake analysis

A confocal laser microscope was used to observe *in vitro* cellular uptake of Cy5.5-labeled GCuNPs and CuNPs in the HK-2 cells. $3x10^5$ HK-2 cells were seeded onto 35 mm cell culture dishes and stabilized for 24 h at 37 °C with 5 % CO_2. Subsequently, equal amounts of Cy5.5-labeled GCuNPs and CuNPs (10 μg/ml of Cu) were treated to HK-2 cells for predetermined time points (1, 3, 6, and 24 h) at 37 °C. Then, the HK-2 cells were washed 3 times with DPBS and stained with DAPI after 4 % paraformaldehyde fixation. Finally, the Cy5.5 fluorescence from GCuNPs and CuNPs in the HK-2 cells was observed using a confocal laser scanning microscope equipped with 405 diodes (405 nm), Ar (458, 488, 514 nm), and He-Ne (633 nm) lasers (Leica TCS SP8; Leica Microsystems, Germany).

4.12. Cell viability analysis

The cytotoxicity of GCuNPs and CuNPs was evaluated using a cell counting kit-8 (CCK-8). In brief, HK-2 cells were seeded onto 96-well plates at a density of 5×10^4 cells per well and stabilized for 24 h at 37 °C with 5 % CO_2. Then, various concentrations of GCuNPs and CuNPs (0.75, 1.5, 3, 6.25, 12.5, 25 μg/ml of Cu) were treated for 24 h at 37 °C. Afterward, the medium was replaced with fresh cell culture medium containing 10 % (v/v) CCK-8 solution and further incubated at 37 °C for 2 h. Finally, the cell viability of each well was calculated using an absorbance at 450 nm measured by a microplate reader (GloMax; GM3500, Promega, USA).

4.13. Intracellular ROS scavenging analysis

To evaluate the intracellular ROS scavenging effect of GCuNPs and CuNPs, HK-2 cells with a density of 3×10^5 were seeded onto 35 mm cell culture dishes and stabilized for 24 h at 37 °C with 5 % CO_2. After stabilization, various concentrations of GCuNPs and CuNPs (1, 5, and 10 μg/ml of Cu)-containing fresh mediums were treated with HK-2 cells for 24 h, and then the mediums were replaced with 2 mM of H_2O_2-containing mediums for 1 h. Afterward, HK-2 cells were washed 3 times with DPBS and were treated with 10 μM of DCFH-DA-containing fresh Opti-MEM™ medium to visualize intracellular ROS for 45 min. The fluorescence of DCFH-DA (λ_{ex}: 505 nm, λ_{em}: 525 nm) was visualized and quantified using a confocal laser scanning microscope and a CytoFLEX flow cytometer (Beckman Coulter, USA).

In addition, cell viability changes of HK-2 cells by ROS scavenging were evaluated using CCK-8. In brief, HK-2 cells with a density of 5×10^4 were seeded onto 96-well plates and stabilized for 24 h at 37 °C with 5 % CO_2. After stabilization, various concentrations of GCuNPs and CuNPs (1, 5, and 10 μg/ml of Cu)-containing fresh mediums were treated with HK-2 cells for 24 h, and then the mediums were replaced with 2 mM of H_2O_2-containing mediums for 1 h. Afterward, the medium was replaced with fresh cell culture medium and further incubated for 24 h. Finally, 10 % (v/v) CCK-8 solution was added to the medium and further incubated at 37 °C for 2 h. The cell viability of each well was calculated using an absorbance at 450 nm measured by a multimode plate reader.

4.14. Biosafety analysis

Based on a previous report, the RBC hemolysis assay was performed to evaluate the *in vivo* hemocompatibility of GCuNPs and CuNPs [69]. The fresh mouse blood was collected and treated with EDTA, and then the RBCs were washed three times with PBS. Afterward, RBCs were isolated from blood by centrifugation at 500*g* for 10 min. RBC pellet was re-dispersed using 500 μl of PBS. 100 μl of RBCs were mixed with a pre-determined concentration of GCuNPs or CuNPs (1.8, 3.75, 7.5, and 15 μg/ml of Cu) for 3 h at 37 °C. The mixtures were centrifuged to separate RBC, and then the absorbance of the supernatant was measured at 540 nm using a multimode plate reader. The hemolysis rate was calculated using the following equation: absorbance of supernatant from RBCs dispersed in PBS was used as the negative control, and absorbance of supernatant from RBCs dispersed in DIW was used as the positive control.

$$Hemolysis\ rate\ (\%) = \left(Abs_{sample} - Abs_{negative}\right) / \left(Abs_{positive} - Abs_{negative}\right) \times 100$$

Next, we evaluated repeated dose toxicity by treating mice five times with CuNPs or GCuNPs (1 mg/kg of Cu) over 12 days. At 14 days after treatment, all mice were sacrificed, and major organs—liver, lung, spleen, kidney, and heart—were excised. The tissues were then fixed in 4% formalin, embedded in paraffin, and stained with hematoxylin and eosin (H&E) for histological analysis. After staining, the tissue slides were examined, and images were captured using an optical microscope (Olympus BX51, Japan).

4.15. Establishment of Cis-induced AKI mice model

All animal experiments were carried out in compliance with the guidelines of the Institutional Animal Care and Use Committee (IACUC) of the Korea Institute of Science and Technology (KIST) (Approval number: KIST-IACUC-2024-061-1). Five-week-old male Balb/c mice were purchased from NaraBio (Gyeonggi-do, South Korea) and used for therapeutic efficacy studies. Five-week-old male Balb/c nude mice were used for biodistribution studies. The cisplatin-induced AKI mouse model was established by a single intraperitoneal injection of high-dose cisplatin (30 mg/kg). Mice that received a saline injection served as

controls. Five-week-old male Balb/c nude mice were used for biodistribution studies.

4.16. Biodistribution analysis on mice

Using optical fluorescence imaging, the biodistribution of GCuNPs and CuNPs was observed in Cis-induced AKI mice and healthy mice. In brief, 5 mg/kg of Cy5.5-labeled GCuNPs and CuNPs were intravenously injected via the tail vein of AKI mice and healthy mice. The fluorescence signal from the whole body of each mouse was monitored at the predetermined time point (1, 3, 6, and 24 h) using the IVIS Lumina Series III optical imaging system (Revvity, Waltham, MA, USA). After 24 h post-injection, the kidney and other major organs (liver, lung, spleen, and heart) were excised from the mice. Then, fluorescence signals from the organs were monitored using the IVIS Lumina Series III optical imaging system. The fluorescence signals from mice and organs were quantified using Living Image® software (Revvity, Waltham, MA, USA), and the values were presented as means ± standard deviation for groups of at least 5 animals.

To further observe the accumulation and distribution of GCuNPs and CuNPs in the kidney, kidney tissues were collected from Cis-induced AKI mice and healthy mice after 6 h post-intravenous injection of Cy5.5-labeled GCuNPs and CuNPs. For frozen sections, kidneys were fixed with 4% paraformaldehyde for 1 h, incubated in 30 % (v/v) sucrose in PBS at 4 °C overnight, and then embedded in optimal cutting temperature (O.C.T.) compound (Sakura FineTek Japan Co., Ltd., Japan). 10 μm-thick tissue slices were stained with FITC-conjugated Occludin monoclonal antibody (33-1511, Invitrogen, USA) at 37 °C for 2 h. Afterward, the tissue slices were washed 3 times with PBS and mounted with a DAPI-containing mounting solution. Finally, the Cy5.5 fluorescence from GCuNPs and CuNPs in the kidney tissues was observed using a confocal laser scanning microscope equipped with 405 diodes (405 nm), Ar (458, 488, 514 nm), and He-Ne (633 nm) lasers (Leica TCS SP8; Leica Microsystems, Germany). The occludin-positive areas for GCuNPs and CuNPs in the fluorescence images were calculated using CellProfiler 4.2.7 software (Broad Institute, USA).

4.17. In vivo therapeutic efficacy analysis on AKI mice

The cisplatin-induced AKI mouse model was established by a single intraperitoneal injection of cisplatin (30 mg/kg). Two hours after cisplatin injection, mice were randomly divided into four groups (n = 5 per group per time point): (1) Ctrl (saline, i.v.), (2) Cis (cisplatin only), (3) Cis(+)CuNPs (CuNPs 250 μg/kg of Cu, i.v.), and (4) Cis(+)GCuNPs (GCuNPs 250 μg/kg of Cu, i.v.). Blood samples were collected from a subset of mice in each group on Day 3 for serum CRE and BUN analysis. Body weight and survival rate were monitored for 7 and 20 days, respectively, to evaluate the short- and long-term therapeutic effects. The remaining mice were sacrificed on Day 7 and Day 20, and kidney tissues were harvested for histological analysis (H&E, PAS, MT staining) and immunofluorescence staining (KIM-1, HO-1).

All mice were monitored daily for body weight changes and clinical signs, including mobility and responsiveness. Humane endpoint decisions were based on an assessment of overall health status. Supportive care, such as hydration and a soft diet, was provided as needed. Any mouse showing a moribund condition was immediately euthanized, regardless of the scheduled experimental endpoint.

4.18. Histological analysis

For paraffin sections, the collected kidney tissues were fixed with 4 % paraformaldehyde and embedded in paraffin. Paraffin-embedded tissues were cut into 8-μm sections. The morphology of kidney tissues was observed after Hematoxylin and Eosin (H&E) stain. PAS staining was performed according to the manufacturer's instructions (PAS stain kit, Abcam, USA). Masson's trichrome staining was performed by DKKorea Co., Ltd. (Seoul, Korea). The % brush border area or % collagen area in the bright field images was semi-quantified using CellProfiler 4.2.7 software (Broad Institute, USA) based on five of 8 consecutive non-overlapping cortical fields of kidney sections stained with PAS and Masson's trichrome under high magnification, respectively.

Kidney sections were deparaffinized in xylene and rehydrated through graded ethanol concentrations. For antigen retrieval, the slides were incubated in citrate buffer (pH 6.0) at 95 °C for 10 min. The slides were permeabilized for 2 min using 0.3% Triton X-100 (sigma) in PBS and then blocked with CAS-Block Histochemical Reagent (Thermo Scientific) for 1 h. Immunofluorescence staining was performed using anti-KIM-1 (1:100, R&D Systems) and anti-HO-1 (1:100, ThermoFisher) overnight at room temperature. The slides were washed three times for 5 min with PBS and then incubated with Alexa Fluor 488 anti-goat or Alexa Fluor 568 anti-rabbit secondary antibodies for 2 h in the dark. After staining the nuclei with 4′,6-Diamidino-2-Phenylindole, Dihydrochloride (DAPI, Invitrogen) for 10 min, the slides were washed three times with distilled water prior to mounting with fluorescence mounting medium (Sigma-Aldrich). Immunofluorescence signals were detected using laser scanning confocal microscope (Leica).

4.19. In vivo biosafety analysis

To evaluate the safety of CuNPs and GCuNPs *in vivo*, histological analysis and blood chemistry analysis were performed after repeated treatment of mice (Balb/c, 5 weeks-old) 5 times with CuNPs or GCuNPs (1 mg/kg of Cu) over 12 days. During the treatment, body weight was monitored every 2 days. At 14 days after treatment, blood was quickly collected by cardiac puncture under anesthesia using a 1 ml syringe with a 25-gauge needle, and then all mice were sacrificed. For blood chemistry analysis, a 500 μl of blood was transferred into a serum separator tube (Becton, Dickinson and Company, Franklin Lakes, NJ, USA). For the separation of serum, the blood sample in the serum separator tube was allowed to form a clot for 1 h at room temperature, followed by centrifugation at 3000 rpm for 10 min at 4 °C. The blood samples and serum samples were analyzed at DKKorea (Seoul, Republic of Korea). For the histological analysis, major organs such as liver, lung, spleen, kidney, and heart were excised. The tissues were then fixed in 4% formalin, embedded in paraffin, and stained with H&E for histological analysis. After staining, the tissue slides were examined, and images were captured using an optical microscope (BX51, Olympus, Tokyo, Japan).

4.20. Statistical analysis

All data were represented as the mean ± standard deviation (S.D.). The results were scrutinized statistically by two-way ANOVA for multiple group comparisons, and the results were analyzed statistically by one-way ANOVA for independent group comparisons using GraphPad Prism 10.3.1 software (GraphPad Software Inc., San Diego, CA, USA). *A p-value* less than 0.05 was considered statistically significant. $^{*}P < 0.05$ was considered statistically significant. $^{**}P < 0.01$, $^{***}P < 0.005$, $^{****}P < 0.001$ were considered highly significant.

CRediT authorship contribution statement

Hokyung Lee: Conceptualization, Methodology, Formal analysis, Investigation, Writing – original draft. **Dahye Noh:** Conceptualization, Methodology, Formal analysis, Investigation, Writing – original draft. **Young Ahn:** Methodology, Formal analysis, Investigation. **Kyeong-Min Lee:** Methodology. **Shin Young Park:** Methodology. **Jiyeon Shin:** Methodology. **Man Kyu Shim:** Methodology. **Sun Hwa Kim:** Formal analysis, Investigation. **Tae Il Noh:** Formal analysis, Investigation. **Hyun-Chul Kim:** Methodology. **Sangmin Lee:** Methodology, Formal analysis, Investigation. **Kwangmeyung Kim:** Methodology. **Hwa Seung Han:** Formal analysis, Investigation, Writing – original draft, Funding

acquisition, Supervision. **Hong Yeol Yoon:** Conceptualization, Formal analysis, Investigation, Writing – original draft, Funding acquisition, Resources, Supervision.

Declaration of competing interest

The authors declare that they have no known competing financial interests or personal relationships that could have appeared to influence the work reported in this paper.

Acknowledgements

This work was supported by the National Research Foundation of Korea (NRF) grant (RS-2024-00355467, RS-2025-02982995) funded by the Korea government (MSIT) and by grants from the Intramural Research Program of the Korea Institute of Science and Technology (2E3375I). It was also supported by the DGIST Start-up Fund Program (2026010340) and DGIST R&D Program (26-NT-01) of the Ministry of Science and ICT.

Appendix A. Supplementary data

Supplementary data to this article can be found online at https://doi.org/10.1016/j.mtnano.2026.100828.

Data availability

Data will be made available on request.

References

[1] S. Dasari, P.B. Tchounwou, Eur. J. Pharmacol. 740 (2014) 364.
[2] H. Luo, G. Yi, H. Tang, L. Chen, L. Hu, D. Yang, Z. Chen, H. Li, D. Zhan, Y. Yu, Y. Zeng, Y. Cai, J. Wu, H. Liu, Sci. Rep. 14 (2024) 18839.
[3] C.D. Barton, B. Pizer, C. Jones, L. Oni, M. Pirmohamed, D.B. Hawcutt, Pediatr. Nephrol. 33 (2018) 1467.
[4] A. Ozkok, C.L. Edelstein, BioMed Res. Int. 2014 (2014) 967826.
[5] R. Murugan, J.A. Kellum, Nat. Rev. Nephrol. 7 (2011) 209.
[6] Y. Ren, F. Wu, L. Huo, X. Wang, Y. Zhang, M. Fan, M. Tan, J. Zhao, J. Cheng, Z. Zhao, J. Bao, Mater. Today Bio 29 (2024) 101328.
[7] M. Ostermann, N. Lumlertgul, R. Jeong, E. See, M. Joannidis, M. James, Lancet 405 (2025) 241.
[8] H. Rashid, A. Jali, M. S. Akhter, S. A. Abdi, Int. J. Mol. Sci., 10.3390/ijms25010003.
[9] B.B. Ratliff, W. Abdulmahdi, R. Pawar, M.S. Wolin, Antioxid. Redox Signaling 25 (2016) 119.
[10] P. Jia, X. Wu, T. Pan, S. Xu, J. Hu, X. Ding, EBioMedicine 49 (2019) 331.
[11] D.-Y. Zhang, H. Liu, K.S. Zhu, T. He, M.R. Younis, C. Yang, S. Lei, J. Wu, J. Lin, J. Qu, P. Huang, J. Nanobiotechnol. 19 (2021) 266.
[12] D.-Y. Zhang, T. Tu, M.R. Younis, K.S. Zhu, H. Liu, S. Lei, J. Qu, J. Lin, P. Huang, Theranostics 11 (2021) 9904.
[13] S. Lin, Y. Cheng, H. Zhang, X. Wang, Y. Zhang, Y. Zhang, L. Miao, X. Zhao, H. Wei, Small 16 (2020) 1902123.
[14] R.-X. Liu, R.-Y. Luo, M.-T. Tang, Y.-C. Liu, Z.-F. Chen, H. Liang, J. Inorg. Biochem. 218 (2021) 111390.
[15] Y. Liu, Y. Qing, L. Jing, W. Zou, R. Guo, Langmuir 37 (2021) 7364.
[16] O. Purikova, I. Tkachenko, B. Šmíd, K. Veltruská, T.N. Dinhová, M. Vorokhta, V. Kopecký Jr., L. Hanyková, X. Ju, Adv. Funct. Mater. 32 (2022) 2208316.
[17] X. Li, Z. Han, T. Wang, C. Ma, H. Li, H. Lei, Y. Yang, Y. Wang, Z. Pei, Z. Liu, Biomaterials 291 (2022) 121904.
[18] C. Wang, J. Xie, X. Dong, L. Mei, M. Zhao, Z. Leng, H. Hu, L. Li, Z. Gu, Y. Zhao, Small 16 (2020) 1906915.
[19] D. Chen, C. Wang, H. Yu, G. Liu, B. Qian, B. Chen, Z. Li, Y. Zhou, S. Pan, B. Li, ACS Appl. Nano Mater. 6 (2023) 13155.
[20] G. Tarricone, V. Castagnola, V. Mastronardi, L. Cursi, D. Debellis, D.Z. Ciobanu, A. Armirotti, F. Benfenati, L. Boselli, P.P. Pompa, Nano Lett. 23 (2023) 4660.
[21] C. Li, Y. Wan, J. Yang, C. Feng, J. Liu, Z. Cao, C. Li, P. Wang, X. Wang, Q. Zeng, Int. J. Biol. Macromol. (2024) 135743.
[22] Z. Zhang, Y. Pan, J.-E. Cun, J. Li, Z. Guo, Q. Pan, W. Gao, Y. Pu, K. Luo, B. He, Acta Biomater. 151 (2022) 480.
[23] Z. Zhang, Z. Lu, Q. Yuan, C. Zhang, Y. Tang, J. Mater. Chem. B 9 (2021) 2240.
[24] C.R. DeJulius, B.R. Dollinger, T.E. Kavanaugh, E. Dailing, F. Yu, S. Gulati, A. Miskalis, C. Zhang, J. Uddin, S. Dikalov, Bioconjug. Chem. 32 (2021) 928.
[25] Y. Chen, X. Yang, K. Li, J. Feng, X. Liu, Y. Li, K. Yang, J. Li, S. Ge, ACS Nano 18 (2024) 7024.
[26] S.K. Rajendrakumar, V. Revuri, M. Samidurai, A. Mohapatra, J.H. Lee, P. Ganesan, J. Jo, Y.-K. Lee, I.-K. Park, Nano Lett. 18 (2018) 6417.
[27] F. Xia, X. Hu, B. Zhang, X. Wang, Y. Guan, P. Lin, Z. Ma, J. Sheng, D. Ling, F. Li, Small 18 (2022) 2201558.
[28] B. Du, M. Yu, J. Zheng, Nat. Rev. Mater. 3 (2018) 358.
[29] D.-Y. Zhang, H. Liu, T. He, M.R. Younis, T. Tu, C. Yang, J. Zhang, J. Lin, J. Qu, P. Huang, Small 17 (2021) 2005113.
[30] D.-Y. Zhang, H. Liu, M.R. Younis, S. Lei, C. Yang, J. Lin, J. Qu, P. Huang, Chem. Eng. J. 409 (2021) 127371.
[31] D.-Y. Zhang, M.R. Younis, H. Liu, S. Lei, Y. Wan, J. Qu, J. Lin, P. Huang, Biomaterials 271 (2021) 120706.
[32] J. Gale, E. Aizenman, Eur. J. Neurosci. (2024).
[33] V. Molahalli, A. Sharma, K. Bijapur, G. Soman, A. Shetty, B. Sirichandana, B.G. M. Patel, N. Chattham, G. Hegde, Copper-Based Nanomaterials in Organic Transformations, vol. 1466, American Chemical Society, 2024, 1.
[34] T. Cherian, C. Ragavendran, R.K.V. Remesh, J. Jacob, W. Jamal, C. Kamaraj, I. Nakouti, J. Environ. Chem. Eng. 11 (2023) 111051.
[35] D. Noh, H. Lee, S. Lee, I.-C. Sun, H. Y. Yoon, Biomater. Res., 28, 94.
[36] Y. Yu, Z. Luo, D.M. Chevrier, D.T. Leong, P. Zhang, D.-e. Jiang, J. Xie, J. Am. Chem. Soc. 136 (2014) 1246.
[37] Y. Yu, X. Chen, Q. Yao, Y. Yu, N. Yan, J. Xie, Chem. Mater. 25 (2013) 946.
[38] Q. Yao, M. Zhu, Z. Yang, X. Song, X. Yuan, Z. Zhang, W. Hu, J. Xie, Nat. Rev. Mater. 10 (2025) 89.
[39] D.M. Chevrier, L. Raich, C. Rovira, A. Das, Z. Luo, Q. Yao, A. Chatt, J. Xie, R. Jin, J. Akola, P. Zhang, J. Am. Chem. Soc. 140 (2018) 15430.
[40] Z. Yang, J. Lyu, J. Qian, Y. Wang, Z. Liu, Q. Yao, T. Chen, Y. Cao, J. Xie, Chem. Sci. 16 (2025) 6542.
[41] X.-C. Dai, M.-H. Huang, Y.-B. Li, T. Li, S. Hou, Z.-Q. Wei, F.-X. Xiao, J. Phys. Chem. C 124 (2020) 4989.
[42] R. Lu, W. Hao, L. Kong, K. Zhao, H. Bai, Z. Liu, RSC Adv. 13 (2023) 14361.
[43] A. Chakravarty, K. Bhowmik, A. Mukherjee, G. De, Langmuir 31 (2015) 5210.
[44] S. Sen, A. Chatterjee, P.K. Maji, J. Mater. Sci.: Composites 7 (2026) 3.
[45] Q. Zhang, J. Wang, Z. Meng, R. Ling, H. Ren, W. Qin, Z. Wu, N. Shao, Nanomaterials 11 (2021) 2258.
[46] S.D. Pike, E.R. White, A. Regoutz, N. Sammy, D.J. Payne, C.K. Williams, M.S. P. Shaffer, ACS Nano 11 (2017) 2714.
[47] X. Han, X. He, L. Sun, X. Han, W. Zhan, J. Xu, X. Wang, J. Chen, ACS Catal. 8 (2018) 3348.
[48] M.C. Biesinger, L.W.M. Lau, A.R. Gerson, R.S.C. Smart, Appl. Surf. Sci. 257 (2010) 887.
[49] Y. Wang, T. Bürgi, Nanoscale Adv. 3 (2021) 2710.
[50] R.D. Vinluan III, J. Liu, C. Zhou, M. Yu, S. Yang, A. Kumar, S. Sun, A. Dean, X. Sun, J. Zheng, ACS Appl. Mater. Interfaces 6 (2014) 11829.
[51] Y. Deng, Y. Gao, T. Li, S. Xiao, M. Adeli, R.D. Rodriguez, W. Geng, Q. Chen, C. Cheng, C. Zhao, ACS Nano 17 (2023) 2943.
[52] J. Park, S. Lee, S. Kim, Front. Chem. 10 (2022) 1030803.
[53] P. Jakubek, K. Suliborska, M. Kuczyńska, M. Asaduzzaman, K. Parchem, I. Koss-Mikołajczyk, B. Kusznierewicz, W. Chrzanowski, J. Namieśnik, A. Bartoszek, Free Radic. Biol. Med. 209 (2023) 239.
[54] Z. Liu, M. Zhang, X. Han, H. Xu, B. Zhang, Q. Yu, M. Li, Chem. Biol. Interact. 252 (2016) 9.
[55] C. Tapeinos, A. Larrañaga, J.-R. Sarasua, A. Pandit, Nanomed. Nanotechnol. Biol. Med. 14 (2018) 2397.
[56] H. Wu, F. Li, S. Wang, J. Lu, J. Li, Y. Du, X. Sun, X. Chen, J. Gao, D. Ling, Biomaterials 151 (2018) 66.
[57] C. Hao, A. Qu, L. Xu, M. Sun, H. Zhang, C. Xu, H. Kuang, J. Am. Chem. Soc. 141 (2019) 1091.
[58] T. Liu, B. Xiao, F. Xiang, J. Tan, Z. Chen, X. Zhang, C. Wu, Z. Mao, G. Luo, X. Chen, J. Deng, Nat. Commun. 11 (2020) 2788.
[59] J. Zeng, C. Ding, L. Chen, B. Yang, M. Li, X. Wang, F. Su, C. Liu, Y. Huang, ACS Appl. Mater. Interfaces 15 (2023) 378.
[60] S.-N. Yin, Y. Liu, C. Zhou, S. Yang, Nanomaterials 7 (2017) 132.
[61] S. Li, Z. Chen, M. Wang, F. Yang, S. Zhang, C. Qiao, W. Chu, W. Yue, ACS Appl. Mater. Interfaces 16 (2024) 3116.
[62] Y. Zheng, H. Yi, Z. Zhan, S.-S. Xue, G. Tang, X. Yu, D.-Y. Zhang, J. Colloid Interface Sci. 662 (2024) 413.
[63] W. Wei, W. Li, L. Yang, S. Weeramantry, L. Ma, P. Fu, Y. Zhao, J. Cell. Physiol. 238 (2023) 727.
[64] X. Ba, T. Ye, H. Shang, Y. Tong, Q. Huang, Y. He, J. Wu, W. Deng, Z. Zhong, X. Yang, ACS Appl. Mater. Interfaces 16 (2024) 12117.
[65] T.M. Hagen, T.Y. Aw, D.P. Jones, Kidney Int. 34 (1988) 74.
[66] M.A. Dobrovolskaia, J.D. Clogston, B.W. Neun, J.B. Hall, A.K. Patri, S.E. McNeil, Nano Lett. 8 (2008) 2180.
[67] L. Tian, H. Feng, Z. Dai, R. Zhang, J. Mater. Chem. B 9 (2021) 53.
[68] S.H. Han, E. Ballinger, S.Y. Choung, J.Y. Kwon, Mar. Drugs 20 (2022).
[69] J.W. Lee, H.Y. Yoon, Y.J. Ko, E.H. Kim, S. Song, S. Hue, N. Gupta, D. Malin, J. Kim, B. Kong, S. Kim, I.-S. Kim, I.C. Kwon, Y. Yang, S.H. Kim, ACS Nano 18 (2024) 22298.